RIS-Enabled Self-Localization With FMCW Radar

Hyowon Kim, *Member, IEEE*, Navid Amani, Musa Furkan Keskin, *Member, IEEE*, Zhongxia Simon He, *Senior Member, IEEE*, Jorge Gil, Gonzalo-Seco Granados, *Fellow, IEEE*, and Henk Wymeersch, *Fellow, IEEE*

***Abstract*—In the upcoming vehicular networks, reconfigurable intelligent surfaces (RISs) are considered as a key enabler of user self-localization without the intervention of the access points (APs). In this paper, we investigate the feasibility of RIS-enabled self-localization with no APs. We first develop a digital signal processing (DSP) unit for estimating the geometric parameters such as the angle, distance, and velocity and for RIS-enabled self-localization. Second, we set up an experimental testbed consisting of a Texas Instrument frequency modulated continuous wave (FMCW) radar for the user, and a Sivers transceiver module that emulates RIS-like directional reflections via analog beam steering and signal loopback. While the Sivers module is not a passive RIS, it enables a controlled emulation of RIS behavior suitable for experimental evaluation. Our results confirm the validity of the developed DSP unit and demonstrate the feasibility of RIS-enabled self-localization using analog RIS emulation.**

***Index Terms*—Channel parameters estimation, frequency modulated continuous wave radar, localization, reconfigurable intelligent surface.**

I. Introduction

Navigation, especially in unknown areas without access to global navigation satellite systems, presents a significant challenge [1], [2]. Simultaneous localization and mapping (SLAM) offers a promising solution by allowing a system to map and localize itself simultaneously in real-time [3], [4]. However, traditional simultaneous localization and mapping (SLAM) systems heavily rely on optical sensors like cameras or LiDAR, which are limited in vision-denied environments—conditions such as smoke-filled rooms, darkness, or areas with poor visibility [5], [6], [7]. These are conditions commonly encountered by first responders during rescue missions or in industrial environments [7].

To address these limitations, FMCW radar has emerged as a viable alternative [8], [9]. Unlike optical sensors, FMCW radar can operate reliably under various weather conditions, including fog, rain, or dust [10]. It has already been successfully adopted for autonomous vehicles and robotics [11], making it a potential solution for SLAM in harsh or low-visibility environments [12]. Radar odometry enhances SLAM by analyzing features in the environment, such as static objects like walls, through consecutive radar scans. By matching environmental features across several radar scans, radar odometry can estimate the movement of a vehicle or robot [13]. Recent advances in RISs have opened new possibilities for wireless positioning. In contrast to traditional approaches that rely on natural features or fixed infrastructures, RISs can serve as controllable and artificial landmarks. The RIS-assisted localization works are growing by exploring deployment scenarios, estimation methods, and hardware assumptions. The works such as [14], [15], [16] explored range or angle estimation using externally observed RIS reflections, including designs that incorporate Cramér-Rao lower bounds (CRLB)-based phase profiles [16] or RIS-assisted sensing [15]. Techniques to mitigate inference [17] and resolve multipath [18] have also been proposed, while the role of RIS placement with double-bounce signals is studied [19]. RIS-enabled geometric localization methods have been proposed, where user positions are estimated via angle-of-arrival (AoA) and time-of-arrival (ToA) from reflected paths [20]. The authors derive positioning bounds under CRLB analysis [21]. Dual-RIS cascaded architectures are introduced in [22] to improve geometric diversity, and RIS-only reflections can enable localization in non line-of-sight (NLOS) settings [23]. A shift toward self-localization emerges in [24], where a user transmits probing signals and processes RIS reflections using time-domain coding. This concept is extended in [25] to a SLAM setting, enabling user-side mapping and positioning without APs. Additional contributions include joint beamforming designs for localization and synchronization [26], and tracking of RIS-equipped vehicles [27]. Meanwhile, learning-based approaches leverage RIS fingerprints via neural networks [28], [29]. Rather than relying solely on natural features for localization, we propose to leverage RIS as artificial landmarks to enhance *radar self-localization* in SLAM as well as multi-target tracking applications. Although RISs have been extensively studied in the context of radar-like sensing of *passive* objects in monostatic [14], [15], [16], [17], [18], [19], bistatic [20], [21], [22] and multistatic [23] configurations. Such approaches require external infrastructure. The use in self-localization of an *active* transmitting device (i.e., a full-duplex radar) remains relatively under-explored, e.g., [24], [25]. To support self-localization of active devices, recent works [24], [25] introduce RIS-aided radar architectures. RISs as artificial landmarks can be strategically placed in the environment, offering consistent and reliable reference points for radar systems [24], [30]. Moreover, such RIS-assisted self-localization solution obviates the need for additional costly infrastructure such as APs or base stations (BSs) [31], [32] and provides a cost-effective strategy to implement radio SLAM [25].While RIS-assisted self-localization has been theoretically investigated in [24], [25], its feasibility has not been demonstrated in a real-world experimental setup.

In this paper, we aim to bridge this gap by designing an experimental setup for RIS-aided self-localization of a monostatic FMCW radar

Received 28 December 2024; revised 29 April 2025; accepted 2 June 2025. Date of publication 17 June 2025; date of current version 20 November 2025. This work was supported in part by the Chalmers Transport Area of Advance, in part by Swedish Research Council under Grant 2022-03007, Grant 2023-05184, and Grant 2024-04390, in part by AGAUR-ICREA Academia Program, in part by the Spanish Agency of Research through MICIU/AEI/10.13039/501100011033 and ERDF/EU under Grant PID2023-152820OB-I00, in part by the National Research Foundation of Korea through the Ministry of Science and ICT under Grant RS-2024-00464570, in part by Advanced Digitalization program at the WiTECH Centre Discourse, and in part by VINNOVA . The review of this article was coordinated by Dr. Hongliang Zhang. *(Corresponding author: Hyowon Kim.)*

Hyowon Kim is with the Department of Electronics Engineering, Chungnam National University, Daejeon 34134, South Korea (e-mail: hyowon.kim@cnu.ac.kr).

Navid Amani, Musa Furkan Keskin, and Henk Wymeersch are with the Department of Electrical Engineering, Chalmers University of Technology, 41296 Gothenburg, Sweden (e-mail: anavid@chalmers.se; furkan@chalmers.se; henkw@chalmers.se).

Zhongxia Simon He is with the School of Cyberspace Science and Technology, Beijing Institute of Technology, Beijing 100811, China, and also with Chalmers Industriteknik, 41258 Göteborg, Sweden (e-mail: zhongxia@bit.edu.cn).

Jorge Gil is with the Department of Architecture and Civil Engineering, Chalmers University of Technology, 41296 Gothenburg, Sweden (e-mail: jorge.gil@chalmers.se).

Gonzalo-Seco Granados is with Universitat Autonoma de Barcelona, 08193 Barcelona, Spain (e-mail: gonzalo.seco@uab.cat).

Digital Object Identifier 10.1109/TVT.2025.3580602

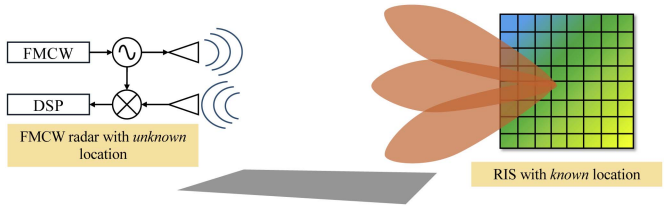

Fig. 1. Considered scenario where an FMCW radar is localized using an RIS.

(shown in Fig. 1), accompanied by algorithms for RIS beam scanning, distance and angle-of-departure (AoD) estimation for localization, and a simulator calibrated to match experimental results and evaluate performance under a wide range of realistic conditions. Our specific contributions are: *(i)* We develop a method tailored for RIS-aided self-localization, allowing real-time estimation of critical geometric parameters such as AoD, distance, and velocity in a monostatic radar configuration; *(ii)* We construct a comprehensive experimental testbed, incorporating an FMCW radar from Texas Instruments [33] to emulate the user equipment (UE) and a transceiver from Sivers [34] to emulate the RIS, to validate the proposed self-localization approach under realistic conditions; *(iii)* We evaluate the feasibility and accuracy of RIS-enabled self-localization through experimental data analysis, and develop a simulator calibrated with this data to investigate system performance under various scenarios, including changes in transmit power, RIS sweep step size, and RIS array dimensions.

II. System Model

We consider a full-duplex UE and a passive RIS. The RIS is equipped with a uniform planar array (UPA) composed of $N_{\text{RIS}} = N_{\text{RIS}}^{\text{az}} \times N_{\text{RIS}}^{\text{el}}$ radiating elements, which lies on the xz plane, and the UE is equipped with a single antenna. Both UE and RIS are static. The UE location is denoted by $\mathbf{x}_{\text{UE}}$. The geometric center of elements at the RIS is denoted by $\mathbf{x}_{\text{RIS}}$ and the location of the n-th element is denoted by $\mathbf{x}_{\text{RIS}}^{n}$.

The UE transmits the chirp signals, and the RIS reflects the signals by controlling the RIS phases, performing a sweeping action across the angular range. The other surrounding objects reflect the transmitted signals. Then, the UE receives multipath due to reflection or scattering in the propagation environment consisting of the RIS and other objects. The analog-to-digital converter (ADC) sample, chirp, RIS sweep angle, and signal path are respectively indexed by n, k, m, and l. The beat signal at the intermediate frequency (IF) for the m-th RIS sweep angle is denoted by $\mathbf{Y}_m$ whose element $[\mathbf{Y}_m]_{n,k}$ indicates the signal on the n-th sample for each k-th chirp, given by [10]

$$[\mathbf{Y}_m]_{n,k} = \gamma_0 e^{-j2\pi(S\tau_0+f_c\nu_0)nT_s} e^{-j2\pi f_c\nu_0 kT} \mathbf{a}^\top(\boldsymbol{\theta})\boldsymbol{\Omega}_m \mathbf{a}(\boldsymbol{\theta}) + \sum_{l=1}^{L} \gamma_l e^{-j2\pi(S\tau_l+f_c\nu_l)nT_s} e^{-j2\pi f_c\nu_l kT} + w_{n,k,m}, \quad (1)$$

where the index $l = 0$ indicates the reflected signals from the RIS and $l > 0$ for the reflected signals from the other objects, the total number of signal paths is $L+1$, γ_l is the complex path gain, $\mathbf{a}(\boldsymbol{\theta}) \triangleq \exp(j\mathbf{X}_{\text{RIS}}^\top \mathbf{g}(\boldsymbol{\theta}))$ denotes the array vector at the RIS with $\boldsymbol{\theta} \triangleq [\theta^{\text{az}}, \theta^{\text{el}}]^\top$ being the AoA and AoD at the RIS,[1] $\mathbf{g}(\boldsymbol{\theta}) \triangleq \frac{2\pi}{\lambda}[\cos(\theta^{\text{az}})\sin(\theta^{\text{el}}), \sin(\theta^{\text{az}})\sin(\theta^{\text{el}}), \cos(\theta^{\text{el}})]^\top$ is the wavenumber vector, $\lambda = c/f_c$ is the wavelength, c is the speed of light, f_c is the carrier frequency, $\mathbf{X}_{\text{RIS}} \triangleq [\mathbf{x}_{\text{RIS}}^1, \ldots, \mathbf{x}_{\text{RIS}}^{N_{\text{RIS}}}]$, $\boldsymbol{\Omega}_m = \text{diag}(\boldsymbol{\omega}_m)$ is the RIS phase matrix, and $\boldsymbol{\omega}_m \triangleq \exp(-2j\mathbf{X}_{\text{RIS}}^\top \mathbf{g}(\boldsymbol{\phi}_m))$ is the RIS phase profile vector whose elements lie on the unit circle with $\boldsymbol{\phi}_m \triangleq [\phi_m^{\text{az}}, \phi_m^{\text{el}}]^\top$ being the parameter vector corresponding to the m-th sweep angle at the RIS. During m-th sweep angle, i.e., seen as a frame, K chirps are transmitted, and each chirp consists of N ADC samples. Furthermore, $S = B/T$ denotes the chirp slope, B is the sweep bandwidth, T is the chirp duration, T_s is the sample duration, $\tau_l = 2d_l/c$ is the round-trip time delay, d_l is the true distance between the UE and object producing the l-th reflection, whose radial velocity is defined as follows: for the RIS path ($l = 0$), $v_l = \mathbf{v}^\top \mathbf{x}_{\text{RU}}/\|\mathbf{x}_{\text{RU}}\|$, where $\mathbf{x}_{\text{RU}} = \mathbf{x}_{\text{RIS}} - \mathbf{x}_{\text{UE}}$; for other paths ($l \neq 0$), $v_l = \mathbf{v}^\top \mathbf{x}_{\text{OU},l}/\|\mathbf{x}_{\text{OU},l}\|$, where $\mathbf{x}_{\text{OU},l} = \mathbf{x}_{\text{O}} - \mathbf{x}_{\text{U}}$. Here, $\mathbf{v}$ denotes the velocity vector of the UE, and $\mathbf{x}_{\text{OU},l}$ is the location of the object that introduces l-th signal path. Hence, $\nu_l = 2v_l/c$ is the corresponding Doppler shift, $w_{n,k,m} \sim \mathcal{CN}(0, \sigma_{\text{N}}^2)$ is the complex Gaussian noise, and σ_{N}^2 is the signal noise covariance.[2]

III. RIS-Enabled Self-Localization

This section describes the signal processing at the FMCW receiver.

A. Delay and Doppler Spectrum

To jointly estimate the distance and radial velocity, we apply the two-dimensional (2D) discrete Fourier transform (DFT) to the beat signal (1) for the sample and chirp dimensions, generating the FMCW delay-Doppler spectrum as described below. We first utilize windowing on the signals

$$\bar{\mathbf{Y}}_m = \mathbf{w}_N \mathbf{w}_K^\top \odot \mathbf{Y}_m, \quad (2)$$

where $\mathbf{w}_A$ is the window vector with A samples and $\odot$ denotes the Hadamard (element-wise) product. To increase the estimation accuracy in 2D DFT, we adopt the zero padding

$$\mathbf{Y}'_m = \begin{bmatrix} \bar{\mathbf{Y}}_m & \mathbf{0}_{N\times(K_{\text{DFT}}-K)} \\ \mathbf{0}_{(N_{\text{DFT}}-N)\times K} & \mathbf{0}_{(N_{\text{DFT}}-N)\times(K_{\text{DFT}}-K)} \end{bmatrix}, \quad (3)$$

where N_{DFT} and K_{DFT} are respectively the number of DFT samples for ADC samples and chirps. For the different RIS beam sweep angles, i.e., $m = 1, \ldots, M$, we generate the delay-Doppler map with the 2D DFT

$$z_m(\tau, \nu) = \sum_{k=0}^{K_{\text{DFT}}-1} \sum_{n=0}^{N_{\text{DFT}}-1} [\mathbf{Y}'_m]_{n,k} e^{j2\pi S\tau nT_s} e^{j2\pi f_c \nu kT}. \quad (4)$$

B. Geometric Parameter Estimation

We estimate the following geometric parameters: AoD from the RIS, distance between the UE and RIS, and Doppler shift at the UE. The geometric parameters are estimated as follows. First, we determine the delay and Doppler pairs for the different RIS beam sweep angles, i.e., $m = 1, \ldots, M$,

$$(\tau_m, \nu_m) = \underset{\tau,\nu}{\text{argmax}} \; |z_m(\tau, \nu)|^2, \quad (5)$$

Second, we estimate the AoD at the RIS by RIS beam sweeping. The received power for each beam is determined by $\hat{m} = \text{argmax}_m P_{\text{ave},m}$, where

$$P_{\text{ave},m} = \frac{1}{2\Delta} \int_{\tau_m-\Delta}^{\tau_m+\Delta} |z_m(\tau, \nu_m)|^2 \text{d}\tau, \quad (6)$$

[1] In monostatic systems, the AoA at an object is the same as the AoD.

[2] We define clutter as (i) unintended reflections that are not distinguishable as separate signal paths, or (ii) false alarms that do not correspond to any meaningful target. These components are absorbed into the Gaussian noise.

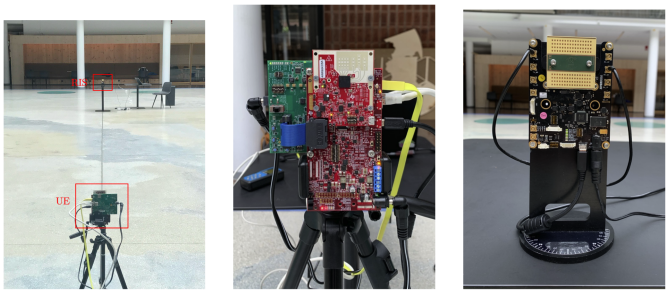

(a) (b) (c)

Fig. 2. Experiment environment, where UE and RIS emulator are deployed: (a) displacement of UE and RIS emulator; (b) UE; and (c) RIS emulator.

where Δ is a design parameter. The estimated AoD $\hat{\boldsymbol{\theta}} \triangleq [\hat{\theta}^{\text{az}}, \hat{\theta}^{\text{el}}]^\top$ is the $\hat{m}$-th RIS beam $\hat{\boldsymbol{\theta}} = \boldsymbol{\phi}_{\hat{m}}$. Finally, the distance and Doppler are estimated by selecting $\hat{m}$-th delay and Doppler pair, i.e., $(\hat{\tau}, \hat{\nu}) = (\tau_{\hat{m}}, \nu_{\hat{m}})$, and the estimated distance and Doppler are determined by $\hat{d} = \hat{\tau}c/2$ and $\hat{v} = \hat{\nu}c/2$, respectively.

C. Localization

We estimate the UE location by exploiting the estimated distance $\hat{d}$ and RIS AoD $\hat{\boldsymbol{\theta}}$. The estimated UE location is

$$\mathbf{x}_{\text{UE}} = \mathbf{x}_{\text{RIS}} + \hat{d}\mathbf{g}(\hat{\boldsymbol{\theta}}), \tag{7}$$

where $\mathbf{g}(\hat{\boldsymbol{\theta}}) = [\cos(\hat{\theta}^{\text{az}})\sin(\hat{\theta}^{\text{el}}), \sin(\hat{\theta}^{\text{az}})\sin(\hat{\theta}^{\text{el}}), \cos(\hat{\theta}^{\text{el}})]^\top$.

IV. Experimental and Simulation Setup

A. Experimental Testbed

Our experimental testbed for RIS-enabled self-localization is depicted in Fig. 2. We deploy the UE and RIS emulator in a large hall, separated by a clear line-of-sight (LOS) path at a distance of approximately 14 meters, as shown in Fig. 2(a). Both are facing each other and located at the same height, indicating that the AoD at the RIS is set to $\boldsymbol{\theta} = [0, 0]^\top$. We emulate the UE by the FMCW radar evaluation kit (AWR6843ISK) from Texas Instruments (TI) (see, Fig. 2(b)), and RIS by a beamforming-capable mmWave transceiver module from Sivers (see, Fig. 2(c)) to mimic RIS beamforming capabilities. Both operate at the frequency of 60 GHz.

To complement the radar module at the UE, we deploy the DCA1000EVM for real-time data capture and streaming. This configuration allows us to seamlessly collect radar data for further processing. We developed an in-house DSP unit using MATLAB, which processes the radar-captured data to extract the relevant experimental results. The Sivers module is equipped with separate transmit (Tx) and receive (Rx) channels, where each consists of 16×4 antenna elements, as illustrated in Fig. 2(c), which allows it to receive radar chirps from the radar module and transmit them back in a specific direction.

To emulate the RIS, we utilize the mmWave transceiver module (Sivers), which we refer to throughout this paper as a *RIS emulator*. While the Sivers module is not a passive RIS in the conventional sense, we repurpose it as a controllable reflector without including any digital baseband processing [35, Fig. 1]. Specifically, the module supports both up- and down-conversion between the radio frequency (RF) (at 60 GHz) and IF (with a 1.2 GHz bandwidth) domains. A 20 GHz local oscillator is multiplied by a factor of three to produce a 60 GHz carrier frequency for up- and down-conversion. This configuration enables directional analog retransmissions that emulate RIS-like beam steering. Importantly, no de-chirping, resampling, or frequency-domain synthesis is applied inside the SiversEVK. As a result, while the reflected bandwidth is limited to 1.2 GHz due to the analog IF chain, the radar remains capable of accurately estimating the target range using de-chirped signals.

This analog loopback introduces a hardware-induced delay, denoted by τ_{RB}, in the signal path, which is not present in a purely passive RIS. While the signal model assumes an idealized round-trip delay τ_0, we note that the actual experimental delay for the $l = 0$ path includes this additional loop-back delay. This delay is consistently accounted for in our experimental analysis as the timing offset between the RIS beam and the RIS body reflection, modeled as

$$\tau_0 = 2\|\mathbf{x}_{\text{UE}} - \mathbf{x}_{\text{RIS}}\|/c + \tau_{\text{RB}}. \tag{8}$$

Therefore, the estimated distance from the delay is computed by $\hat{d} = (\hat{\tau} - \tau_{\text{RB}})c/2$.

The beam-steering functionality of the RIS emulator enables directional re-transmissions within an angle range of -45 to +45 degrees relative to its broadside, making it highly adaptable for our purposes. During the experiment, the UE continuously transmits FMCW chirps, which are received by the Rx channels of the RIS emulator. These signals are then re-transmitted by the RIS emulator at varying scan angles, covering the entire angular range ϕ_m^{az} from -45 to 45 degrees in 1.5-degree increments[3] and $\phi_m^{\text{el}} = 0°$. This configuration allows directional re-transmissions that mimic RIS beam-steering behavior, enabling the radar to associate reflected power with beam angles and estimate the AoD for self-localization. The signal flow between the UE and the RIS emulator proceeds as follows. The FMCW radar at the UE transmits chirp signals. These signals are received by the Sivers module's Rx antenna array. The received RF signal is looped back to the Tx path through a coaxial cable and micro coaxial connectors (shown in Fig. 2(c)). No additional up/downconversion hardware (e.g., USRP) was used in the signal re-transmission. The Sivers module handled the RF signal path entirely. The signal is re-transmitted using the Tx array with analog beam steering, sweeping azimuth angles from $-45°$ to $+45°$ in $1.5°$ steps. The FMCW radar at the UE receives the re-transmitted signal.

To achieve synchronization between the RIS emulator and the UE, we implement a *pre-programmed on–off–on signaling pattern procedure*, which enables proper association of the beam angle at the RIS emulator with the received signal at the UE. While no real-time signaling or physical connection exists between the two devices, both follow a coordinated timing schedule. Specifically, the RIS emulator is turned on with a broadside beam for a fixed duration, turned off briefly, and turned on again to generate a distinct signature in the UE's received power profile. This pattern allows the UE to detect the start of the beam sweep at the RIS emulator and reliably align the received signal with the corresponding beam angle over time, as illustrated in Fig. 4.

While this process takes place, the UE captures samples of the reflected signals at each scan angle. This experimental method allows us to measure the average power at the radar for different beam-steering angles, $P_{\text{ave},m}$ of (6) in dBm. By systematically varying the angles and recording the response of the radar, we estimate the AoD that maximizes the average power $P_{\text{ave},m}$. Treating the RIS emulator as an artificial landmark with a known location allows the radar to accurately

[3]To emulate the RIS beam-steering process with separate Tx and Rx arrays, the Tx beamforming vector at the m-th sweep angle is $\boldsymbol{\omega}_m^{\text{Tx}} = \exp(-j\mathbf{X}_{\text{Tx}}^\top \mathbf{g}(\boldsymbol{\phi}_m))$, defined with the RIS phase matrix of (1). Since the RIS emulator is located at the boresight of the UE for maximum reception, its receive beam is always directed toward the UE and does not change with the Tx beam scanning. Consequently, the Rx beamforming vector is $\boldsymbol{\omega}^{\text{Rx}} = \exp(-j\mathbf{X}_{\text{Rx}}^\top \mathbf{g}(\boldsymbol{\theta}))$. Due to identical arrays, we have $\mathbf{X}_{\text{Tx}} = \mathbf{X}_{\text{Rx}}$.

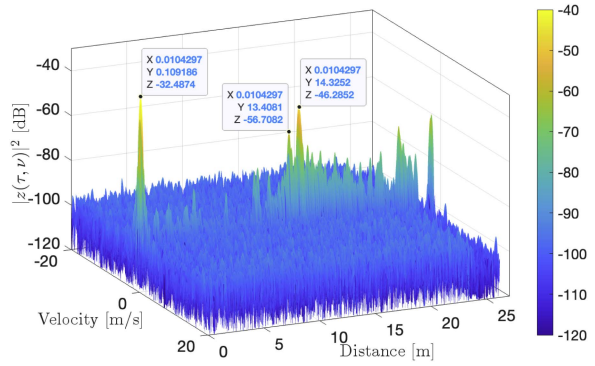

Fig. 3. Three largest peaks in 2D distance and velocity spectrum with the experiment data, obtained by (4) at the $\hat{m}$-th sweep angle corresponding to $\boldsymbol{\phi} = [0°, 0°]^\top$.

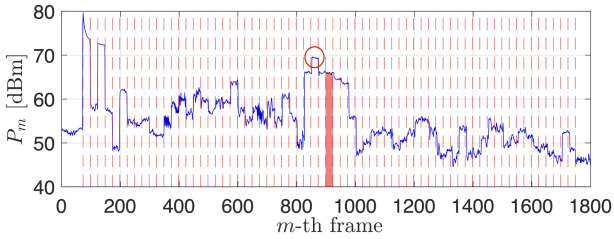

Fig. 4. Example of the AoD estimation ($\hat{\boldsymbol{\phi}} = [-3°, 0°]^\top$ and $\boldsymbol{\phi} = [0°, 0°]^\top$ corresponding to the frames marked by the red circle (estimates) and highlighted by the red bar (true), respectively.).

self-localize, while simultaneously generating environmental images for mapping purposes.

B. Simulation Setup

To validate the designed signal model of (1) and the proposed RIS-enabled self-localization method in Section III, we construct a simulator of our experimental testbed in the MATLAB environment. The goal is to harness the experimental results for calibrating the simulator, which are then employed to investigate performance under a rich set of conditions that cannot be tested with experiments. Instead of real-time signal capturing and streaming, we artificially generate the noisy signal data that follows the received signal model (1). The squared amplitude of complex path gain for the targets (i.e., $l > 0$) is $|\gamma_l|^2 = PG_{\text{trx}}S^l_{\text{RCS}}\lambda^2/((4\pi)^3 d_l^4)$, where P is the transmit power, G_{trx} is the combined transmit and receive antenna gain, S^l_{RCS} is the radar cross section (RCS) of the objects that producing the signal reflection. As to the complex gain of the RIS loopback path ($l = 0$), it involves the impact of both amplification factors due to the active nature of the RIS [36] and the losses incurred during loopback from receive to transmit path in the active RIS: $\zeta = L_{\text{loss}}\alpha_{\text{RIS}}$, where α_{RIS} is the amplification factor common to all the RIS elements [36], [37] and L_{loss} is the loopback loss, both representing unitless quantities. Hence, the squared amplitude of the complex gain of the loopback path can be expressed as [37], [38]

$$|\gamma_0|^2 = PG_{\text{trx}}|\gamma_{\text{UR}}|^2\zeta|\gamma_{\text{RU}}|^2, \tag{9}$$

where γ_{UR} and γ_{RU} denote the gains of the UE-RIS path and the RIS-UE radar path, respectively. We have [37] $|\gamma_{\text{UR}}|^2 = |\gamma_{\text{RU}}|^2 = \lambda^2/(4\pi d_0)^2$, where d_0 is the distance between the UE and the RIS. In the computation of average power (6), the design parameter Δ of (6) is set to 0.33 ns, the time delay corresponding to the distance 0.1 m. We utilize the Hann window function, and the a-th sample of the Hann window vector is $\mathbf{w}_A(a) = \sin^2(a\pi/A)$, where A is the number of samples. The simulation parameters are summarized in Table I. The results are averaged over 1000 simulation runs.

TABLE I
THE SIMULATION PARAMETERS

Parameter	Value
RIS array size	$N_{\text{RIS}} = 64$ (16×4)
Transmission power	$P = 20$ dBm
Combined Tx and Rx antenna gain	$G_{\text{trx}} = 4.7712$ dBi
RCS of the targets (for $l > 0$)	$S^l_{\text{RCS}} = 19$ m^2
Amplification and loss factor	$\zeta = 45.532$ dB
Number of chirps	$K = 128$
Number of ADC samples	$N = 600$
Chirp duration	$T = 50$ ms
Sweep bandwidth	$B = 3.4345$ GHz
IF bandwidth	$B_{\text{IF}} = 10$ MHz
Carrier frequency	$f_c = 60$ GHz
Wavelength	$\lambda = 0.005$ m
Signal noise covariance	$\sigma^2_{\text{N}} = -63.64$ dBm
Loop-back delay at the RIS emulator	$\tau_{\text{RB}} = 1.78$ ns
Number of DFT samples	$N_{\text{DFT}} = 1199$, $K_{\text{DFT}} = 4793$
UE position	$\mathbf{x}_{\text{UE}} = [0, 0]^\top$
RIS position	$\mathbf{x}_{\text{RIS}} = [0, 13.38]^\top$.

V. Results and Discussions

A. Experimental Results

Utilizing the collected experimental data in the testbed, we investigate the 2D distance and velocity spectrum, obtained by (4) at the sweep angle corresponding to $\boldsymbol{\phi}_m = [0, 0]^\top$, shown in Fig. 3. From the 2D spectrum, we see the first three largest peaks, where the first is the self-interference due to the Tx antenna leakage to Rx in monostatic (co-located) radars [39], the second by the physical reflection by the RIS emulator, and the third by the retransmitted signal at the RIS emulator. Therefore, we filter out the first peak and then exploit the parameter estimation method (Section III-B).

Fig. 4 shows the average power over the frames of (6), to estimate the AoD. The true AoD is $\boldsymbol{\phi} = [0°, 0°]^\top$ corresponds to the frames highlighted by the red bar, and estimated AoD $\hat{\boldsymbol{\phi}} = [-3°, 0°]^\top$ corresponds to the frames marked by the red circle. The average power fluctuates sharply in the initial few hundred frames, then gradually increases, and eventually gradually decreases after passing about the midpoint of the frames. This behavior is attributed to the RIS emulator being turned on and off repeatedly during the initial few hundred frames for synchronization purposes, followed by the beam-steering sweep with the angular range from -45° (starting at the 150-th frame) to 45° in increments of 1.5°.

It is worth noting that no baseline comparison is provided, since there is no prior experimental realization of RIS-assisted self-localization in a monostatic configuration.

B. Simulation Results and Extrapolation

To validate the developed DSP unit using MATLAB including the formulated signal model (1) and the proposed geometric parameters estimation method (Section III-B), in Fig. 5, we compare the 1D distance profile results, at $\nu \approx 0$ and $\boldsymbol{\theta} = [0, 0]^\top$. The experiment data is analyzed by the TI mmWave radar (solid line) and by the proposed parameter estimation method (dotted line), which is also applied to the

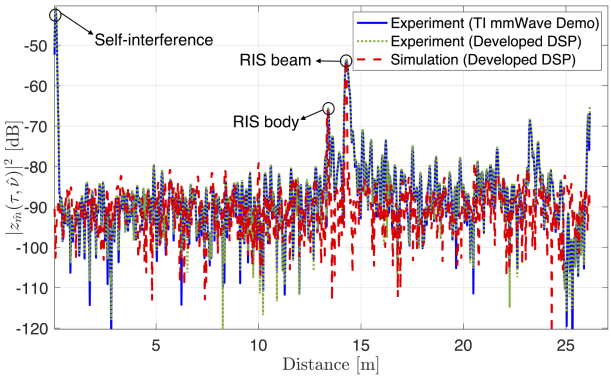

Fig. 5. Comparison of 1D distance profile results with the experiment data by the TI mmWave kit (solid line) and by the proposed parameter estimation method (dotted line), and simulation data by the designed signal model and proposed estimation method (dashed line), at $\nu \approx 0$ and $\boldsymbol{\phi} = [0°, 0°]^\top$ corresponding to the $\hat{m}$-th sweep angle of the RIS emulator.

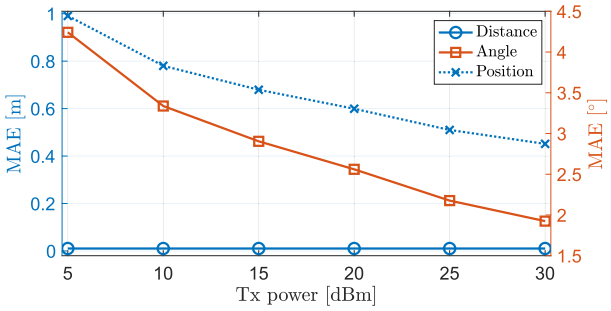

Fig. 6. MAEs of distance, angle, and position estimates with the different Tx powers.

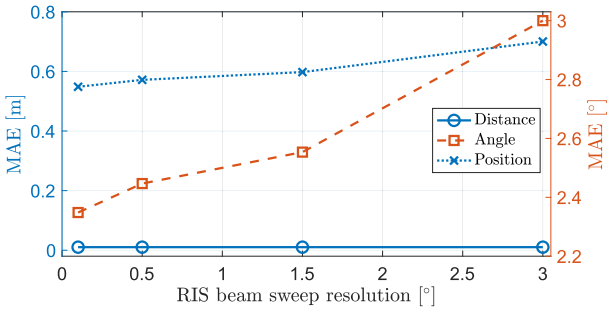

Fig. 7. MAEs of distance, angle, and position estimates with the different beam sweep resolutions of the RIS emulator.

simulation data (dashed line). In the dashed line, the first peak that originated from the reflected signal from the UE itself is absent as this self-interference is not modeled in the simulated data. We demonstrate that the developed DSP is valid as the solid line matches the dotted line, and the dashed line has the same two peaks corresponding to physical reflection at the RIS and retransmitted signal at the RIS, as the solid and dotted lines. In addition to the RIS beam, power fluctuations caused by environmental scatterers located behind the RIS, can be observed in the experimental data. These weak multipath components are not modeled in the simulation data, which explains the deviations between the solid and dashed lines.

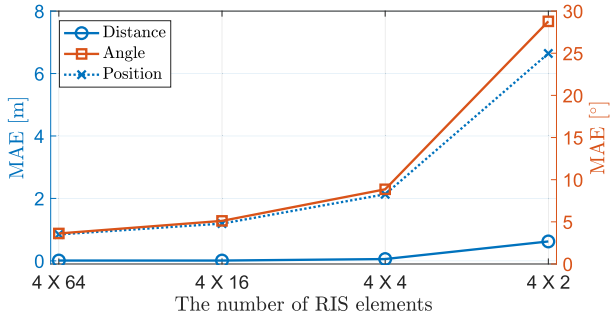

Fig. 8. MAEs of distance, angle, and position estimates with the different number of elements at the RIS emulator.

Figs. 6– 8 show the geometric parameters and positioning estimation errors with the different setup configurations. Fig. 6 presents the results with the different Tx powers. The distance estimation error does not vary for the range of Tx power values for which the peaks of the spectrum can be resolved in the distance dimension with a fixed distance search grid ($N_{\text{DFT}} = 1199$) on the distance profile. We observe a smaller AoD error with the larger Tx power. Due to the smaller AoD error with the larger Tx power, while maintaining the same distance errors, the positioning error also decreases as the Tx power increases. Fig. 7 shows the results with various RIS beam sweep resolutions. The fine beam leads to a smaller AoD estimation error while maintaining the distance estimation error due to the resolvable peaks with a fixed distance search grid on the distance profiles. Therefore, the positioning error decreases with the fine RIS beam sweep resolution. Fig. 8 presents the results with different number of RIS elements. The distance estimation error also decreases with a larger number of RIS elements. This happens because the two peaks corresponding to physical reflection at the RIS and re-transmitted signal at the RIS are resolvable with a larger number of RIS elements. The AoD estimation error decreases as the number of RIS elements increases. Therefore, the positioning error decreases with more RIS elements.

VI. Conclusion

In this paper, we demonstrated the feasibility of RIS-enabled self-localization without AP intervention through both experimental and simulation results. In the experimental testbed, we assessed the developed DSP unit by comparing the 1D distance profile with the TI mmWave radar evaluation kit. We confirmed the validity of our designed signal model, which adheres to the deterministic model, in the signal propagation environment of the 60 GHz FMCW radar. For future work, the feasibility of multiple target tracking and SLAM, with the assistance of RISs, will be further explored. In addition, comprehensive analyses of hardware impairments such as phase deviations (due to oscillator noise, and nonlinearities) and unintended effects from practical beamforming implementations (due to mutual coupling, and side-lobe interference) are planned to be conducted in real-world scenarios.

References

[1] K. -W. Chiang et al., "Seamless navigation and mapping using an INS/GNSS/grid-based SLAM semi-tightly coupled integration scheme," *Inf. Fusion*, vol. 50, pp. 181–196, Oct. 2019.

[2] G. He, X. Yuan, Y. Zhuang, and H. Hu, "An integrated GNSS/LiDAR-SLAM pose estimation framework for large-scale map building in partially GNSS-denied environments," *IEEE Trans. Instrum. Meas.*, vol. 70, 2021, Art. no. 7500709.

[3] H. Durrant-Whyte and T. Bailey, "Simultaneous localization and mapping: Part I," *IEEE Robot. Autom. Mag.*, vol. 13, no. 2, pp. 99–110, Jun. 2006.

[4] T. Bailey and H. Durrant-Whyte, "Simultaneous localization and mapping (SLAM): Part II," *IEEE Robot. Autom. Mag.*, vol. 13, no. 3, pp. 108–117, Sep. 2006.

[5] B. Amjad, Q. Z. Ahmed, P. I. Lazaridis, M. Hafeez, F. A. Khan, and Z. D. Zaharis, "Radio SLAM: A review on radio-based simultaneous localization and mapping," *IEEE Access*, vol. 11, pp. 9260–9278, 2023.

[6] H. A. G. C. Premachandra, R. Liu, C. Yuen, and U. -X. Tan, "UWB radar SLAM: An anchorless approach in vision denied indoor environments," *IEEE Robot. Autom. Lett.*, vol. 8, no. 9, pp. 5299–5306, Sep. 2023.

[7] J. M. Santos et al., "A sensor fusion layer to cope with reduced visibility in SLAM," *J. Intell. Robotic Syst.*, vol. 80, pp. 401–422, Jan. 2015.

[8] A. Venon, Y. Dupuis, P. Vasseur, and P. Merriaux, "Millimeter wave FMCW radars for perception, recognition and localization in automotive applications: A survey," *IEEE Trans. Intell. Veh.*, vol. 7, no. 3, pp. 533–555, Sep. 2022.

[9] S. M. Patole, M. Torlak, D. Wang, and M. Ali, "Automotive radars: A review of signal processing techniques," *IEEE Signal Process. Mag.*, vol. 34, no. 2, pp. 22–35, Mar. 2017.

[10] C. Aydogdu et al., "Radar interference mitigation for automated driving: Exploring proactive strategies," *IEEE Signal Process. Mag.*, vol. 37, no. 4, pp. 72–84, Jul. 2020.

[11] A. N. Ramesh, C. M. Leon, J. C. Zafra, S. Brü ggenwirth, and M. A. González-Huici, "Landmark-based RADAR SLAM for autonomous driving," in *Proc. 21st Int. Radar Symp.*, Jun. 2021, pp. 1–10.

[12] P. Fritsche et al., "Fusing LiDAR and radar data to perform SLAM in harsh environments," in *Proc. 13th Int. Conf. Informat. Control Autom. Robot.*, Lisbon, Portugal, Jul. 2016, pp. 175–189.

[13] D. C. Herraez, M. Zeller, L. Chang, I. Vizzo, M. Heidingsfeld, and C. Stachniss, "Radar-only odometry and mapping for autonomous vehicles," in *Proc. IEEE Int. Conf. Robot. Autom.*, May 2024, pp. 10275–10282.

[14] H. Zhang, H. Zhang, B. Di, K. Bian, Z. Han, and L. Song, "MetaRadar: Multi-target detection for reconfigurable intelligent surface aided radar systems," *IEEE Trans. Wireless Commun.*, vol. 21, no. 9, pp. 6994–7010, Sep. 2022.

[15] X. Shao, C. You, W. Ma, X. Chen, and R. Zhang, "Target sensing with intelligent reflecting surface: Architecture and performance," *IEEE J. Sel. Areas Commun.*, vol. 40, no. 7, pp. 2070–2084, Jul. 2022.

[16] X. Song, J. Xu, F. Liu, T. X. Han, and Y. C. Eldar, "Intelligent reflecting surface enabled sensing: Cramér-Rao bound optimization," *IEEE Trans. Signal Process.*, vol. 71, pp. 2011–2026, 2023.

[17] Z. Xie, L. Wu, J. Zhu, M. Lops, X. Huang, and M. R. B. Shankar, "RIS-aided radar for target detection: Clutter region analysis and joint active-passive design," *IEEE Trans. Signal Process.*, vol. 72, pp. 1706–1723, 2024.

[18] K. Meng, Q. Wu, R. Schober, and W. Chen, "Intelligent reflecting surface enabled multi-target sensing," *IEEE Trans. Commun.*, vol. 70, no. 12, pp. 8313–8330, Dec. 2022.

[19] H. Kim et al., "RIS-aided monostatic sensing and object detection with single and double bounce multipath," in *Proc. IEEE Int. Conf. Commun. Workshops (ICC Workshops)*, Rome, Italy, Jun. 2023, pp. 1883–1889.

[20] S. Buzzi, E. Grossi, M. Lops, and L. Venturino, "Foundations of MIMO radar detection aided by reconfigurable intelligent surfaces," *IEEE Trans. Signal Process.*, vol. 70, pp. 1749–1763, 2022.

[21] Y. Huang, J. Yang, W. Tang, C. -K. Wen, S. Xia, and S. Jin, "Joint localization and environment sensing by harnessing NLOS components in RIS-aided mmwave communication systems," *IEEE Trans. Wireless Commun.*, vol. 22, no. 12, pp. 8797–8813, Dec. 2023.

[22] R. Liu, M. Li, H. Luo, Q. Liu, and A. L. Swindlehurst, "Integrated sensing and communication with reconfigurable intelligent surfaces: Opportunities, applications, and future directions," *IEEE Wireless Commun.*, vol. 30, no. 1, pp. 50–57, Feb. 2023.

[23] W. Lu, Q. Lin, N. Song, Q. Fang, X. Hua, and B. Deng, "Target detection in intelligent reflecting surface aided distributed MIMO radar systems," *IEEE Sensors Lett.*, vol. 5, no. 3, pp. 2475–1472, Mar. 2021.

[24] K. Keykhosravi, G. Seco-Granados, G. C. Alexandropoulos, and H. Wymeersch, "RIS-enabled self-localization: Leveraging controllable reflections with zero access points," in *Proc. IEEE Int. Conf. Commun. Workshops (ICC)*, Seoul, South Korea, May 2022, pp. 2852–2857.

[25] H. Kim et al., "RIS-enabled and access-point-free simultaneous radio localization and mapping," *IEEE Trans. Wireless Commun.*, vol. 23, no. 4, pp. 3344–3360, Apr. 2024.

[26] A. Fascista, M. F. Keskin, A. Coluccia, H. Wymeersch, and G. Seco-Granados, "RIS-aided joint localization and synchronization with a single-antenna receiver: Beamforming design and low-complexity estimation," *IEEE J. Sel. Topics Signal Process.*, vol. 16, no. 5, pp. 1141–1156, Aug. 2022.

[27] S. Aghashahi, Z. Zeinalpour-Yazdi, A. Tadaion, M. B. Mashhadi, and A. Elzanaty, "Single antenna tracking and localization of RIS-enabled vehicular users," *IEEE Trans. Veh. Technol.*, vol. 74, no. 3, pp. 4362–4375, Mar. 2025.

[28] X. Tong, Z. Zhang, J. Wang, C. Huang, and M. Debbah, "Joint multi-user communication and sensing exploiting both signal and environment sparsity," *IEEE J. Sel. Topics Signal Process.*, vol. 15, no. 6, pp. 1409–1422, Nov. 2021.

[29] T. Wu et al., "Exploit high-dimensional RIS information to localization: What is the impact of faulty element?," *IEEE J. Sel. Areas Commun.*, vol. 42, no. 10, pp. 2803–2819, Oct. 2024.

[30] K. Keykhosravi et al., "Leveraging RIS-enabled smart signal propagation for solving infeasible localization problems: Scenarios, key research directions, and open challenges," *IEEE Veh. Technol. Mag.*, vol. 18, no. 2, pp. 20–28, Jun. 2023.

[31] S. Basharat, S. A. Hassan, H. Pervaiz, A. Mahmood, Z. Ding, and M. Gidlund, "Reconfigurable intelligent surfaces: Potentials, applications, and challenges for 6G wireless networks," *IEEE Wireless Commun.*, vol. 28, no. 6, pp. 184–191, Dec. 2021.

[32] H. Chen et al., "RISs and sidelink communications in smart cities: The key to seamless localization and sensing," *IEEE Commun. Mag.*, vol. 61, no. 8, pp. 140–146, Aug. 2023.

[33] S. Rao, "Introduction to mmWave sensing: FMCW radars," *Texas Instrum. (TI) mmWave Training Ser.*, 2017. [Online]. Available: https://www.ti.com/content/dam/videos/external-videos/ko-kr/2/3816841626001/5415203482001.mp4/subassets/mmwaveSensing-FMCW-offlineviewing_0.pdf

[34] S. Semiconductors, "Evaluation kit EVK06002," (n.d.). [Online]. Available: https://www.sivers-semiconductors.com/5g-millimeter-wave-mmwave-and-satcom/wireless-products/evaluation-kits/evaluation-kit-evk06002

[35] I. Aziz et al., "60 GHz RF module with beam-steering optimization algorithm for high data rate access and backhaul communications," *EURASIP J. Wireless Commun. Netw.*, vol. 2022, no. 1, 2022, Art. no. 92.

[36] Z. Zhang et al., "Active RIS vs. passive RIS: Which will prevail in 6G?," *IEEE Trans. Commun.*, vol. 71, no. 3, pp. 1707–1725, Mar. 2023.

[37] E. Grossi, H. Taremizadeh, and L. Venturino, "Radar target detection and localization aided by an active reconfigurable intelligent surface," *IEEE Signal Process. Lett.*, vol. 30, pp. 903–907, 2023.

[38] M. Rihan, E. Grossi, L. Venturino, and S. Buzzi, "Spatial diversity in radar detection via active reconfigurable intelligent surfaces," *IEEE Signal Process. Lett.*, vol. 29, pp. 1242–1246, 2022.

[39] P. Fenske, A. Scheder, T. Koegel, K. Root, M. Vossiek, and C. Carlowitz, "Self-interference leakage estimation 'N'cancellation element: Design of an active self-interference cancellation coupler," *IEEE Microw. Mag.*, vol. 24, no. 6, pp. 68–75, Jun. 2023.